3D Reconstruction and Analysis of Wing Deformation in Free-Flying Dragonflies

Christopher Koehler[1], Zongxian Liang[2], Zachary Gaston[2], Hui Wan[2], Haibo Dong[2]

[1] Department of Computer Science & Computer Engineering, Wright State University, Dayton, OH, 45435, USA

[2] Department of Mechanical & Materials Engineering, Wright State University, Dayton, OH, 45435, USA

SUMMARY

Insect wings demonstrate elaborate three-dimensional deformations and kinematics. These deformations are key to understanding many aspects of insect flight including aerodynamics, structural dynamics and control. In this paper, we propose a template-based subdivision surface reconstruction method that is capable of reconstructing the wing deformations and kinematics of free-flying insects based on the output of a high-speed camera system. The reconstruction method makes no rigid wing assumptions and allows for an arbitrary arrangement of marker points on the interior and edges of each wing. The resulting wing surfaces are projected back into image space and compared with expert segmentations to validate reconstruction accuracy. A least squares plane is then proposed as a universal reference to aid in making repeatable measurements of the reconstructed wing deformations. Using an Eastern Pondhawk, *Erythimus Simplicicollis* dragonfly as a demonstration, we quantify and visualize the wing twist and camber in both the chord-wise and span-wise directions, and discuss the implications of the results. In particular, a detailed analysis of the subtle deformation in the dragonfly's right hindwing suggests that the muscles near the wing root could be used to induce chord-wise camber in the portion of the wing nearest the specimen's body. We conclude by proposing a novel technique for modeling wing corrugation in the reconstructed flapping wings. In this method, displacement mapping is used to combine wing surface details measured from static wings with the reconstructed flapping wings, while not requiring any additional information be tracked in the high speed camera output.

INTRODUCTION

Most of nature's fliers are equipped with flexible wings. Wing flexibility is of interest in both aerodynamics (Combes and Daniel, 2001;Sane, 2003;Wootton, 1993;Zhao et al., 2009;Zhao et al., 2011) and structural dynamics (Combes and Daniel, 2003a;Combes and Daniel, 2003b). It is widely believed that wing flexibility and deformation can potentially provide new mechanisms of aerodynamic force production, which presents itself as passive cambering patterns as a result of wing flexural stiffness, kinematics and fluid structure interactions not present in completely rigid wings (Combes and Daniel, 2001;Sane, 2003).

Insect wings are of particular interest due to their small size and the wide variety of passive cambering patterns they undergo as a result of wing and fluid interaction. In a previous study, (Combes and Daniel, 2003a;Combes and Daniel, 2003b) investigated the role that wing venation plays in these deformations. They showed that wing flexural stiffness varies by four orders of magnitude across insect taxa, wing flexibility strongly correlates with absolute wingspan and that chord length accounts for more than 95% of the observed variation in flexural stiffness for insect wings.

As pointed out by (Walker et al., 2009b), high-speed photogrammetry is more suitable for studying wing deformation than the 'strips' method in which wings are modeled as a series of chord-wise strips (Willmott and Ellington, 1997) because it cannot capture wing camber. It also has advantages over the projected laser line method in which static lasers are used to project a fringe pattern onto flapping wings (Song et al., 2001;Sunada et al., 2002;Wang et al., 2003;Zeng et al., 1996;Zeng et al., 2000) because specific points on the wings cannot be tracked due to the fixed laser alignment.

Photogrammetry was used by (Hedrick and Biewener, 2007) and (Tobalske et al., 2007) to study hummingbird wing kinematics in free-flight and (Lauder et al., 2006) successfully reconstructed details of 3D fish fin kinematics in forward swimming using photogrammetry based reconstructions. In addition (Norberg and Winter, 2006) filmed bats flying in a wind tunnel and demonstrated that bat wing kinematics change predictably with time. Photogrammetric reconstructions of free-flying bats were also used to quantify the effects of flight speed and reconstruction accuracy on the dimensional

complexity observed in reconstructed bat wing kinematics (Riskin et al., 2008). The inertial effects of wing movement in the flapping flight of a fruit bat was also studied previously (Iriarte-Díaz et al., 2011).

More recently photogrammetry has been used to study insect flight, which is more challenging due to the small size, faster flapping rate and the fact that it is not feasible to place large reflective markers (like those used in the studies of bats) on their tiny wings. For instance, (Ristroph et al., 2009) used automated volumetric hull reconstruction on the images output from a photogrammetry system to study sideways free-flight of Drosophila. In addition, (Fontaine et al., 2009) studied free-flying Drosophila using automated model-based tracking for analysis of the wing-body kinematics during voluntary and escape take-offs. However, in both these works, all wings were treated as rigid plates instead of deformable ones due to a lack of spatial resolution, although the importance of deformations in the study of wing kinematics was pointed out in both papers. In another study, (Liu and Sun, 2008) used three orthogonally aligned high-speed cameras to study the wing kinematics and aerodynamics of hovering droneflies. Also, (Walker et al., 2009b) used a four camera photogrammetric system and a combination of manual and semi-automatic tracking of natural features and marker points to reconstruct the wing kinematics and surface topographies of free flying hoverflies and tethered locusts.

Despite some recent quantitative analysis of the wings of tethered (Sunada et al., 2002;Walker et al., 2009a) and free-flying (Bergou et al., 2010;Walker et al., 2010) insects, there is still a lack of literature regarding detailed 3D measurements of wing deformation in both the span-wise and chord-wise directions. This is partially due to the small wing size, fast motion of the wings, and unpredictable movement of free-flying insects. All these factors make high-speed tracking of the details of wing flexion extremely challenging. In most high-speed photogrammetric studies, subjects have been tethered, with few efforts made at capturing true free-flight dynamics. Those who have studied free-flying insects have made assumptions about flexibility such as treating the leading edge as rigid and ignoring span-wise flexibility altogether in their kinematics measurements.

Unsteady effects of wing rotation have previously been established as a key component of force production in insect flight (Dickinson et al., 1999). More recently, several studies have begun to reveal the additional aerodynamic significance of wing deformation details that would not be captured if rigid wing assumptions were made in either insect wing reconstruction or kinematic analysis. For instance, chord-wise camber's role in improving aerodynamic and mechanical performance was investigated by (Du and Sun, 2008;Du and Sun, 2010;Vanella et al., 2009). In addition, (Stanford et al., 2010) demonstrated that span-wise flexibility, a phenomenon that has been almost completely ignored in the study of insect flight, also plays a role in power consumption. Wing flexibility has also been shown to play a role in leading edge vortex stability (Koehler et al., 2011; Zhao et al., 2011). These results highlight the need for insect wing surface reconstruction and deformation analysis methods that capture and utilize all aspects of wing deformation while remaining general enough to be applied to a wide variety of free-flying insects.

Several previous studies have also looked at the mesosurface morphological details, such as corrugation, found in insect wings, however these studies have focused primarily on static wings. Laser scanning was used to measure the surface roughness of severed insect wings (Tsuyuki et al., 2006). The structure of a dragonfly forewing and hindwing were studied by scanning them with a micro-CT scanner (Jongerius and Lentink, 2010). Corrugation in flapping insect wings was also studied (Walker et al., 2009a). This work used a large number of marker points (approximately 100 per hindwing) for a tethered locust. However, tracking a high number of marker points in free-flight studies is undesirable. Currently the relationship between 3D surface corrugation and induced airflow remains unclear. This further motivates the need for a simple method for modeling insect wing surface corrugation in free-flight reconstructions.

This paper presents a unified methodology for the reconstruction and analysis of the deformations and surface morphology exhibited by insect wings during free-flight. The primary goals of the proposed techniques are to eliminate all rigid wing assumptions during the reconstruction and deformation analysis while minimizing the number of tracked points in the output of the photogrammetry system. Also it is desirable for the

methodology to remain general enough to be applied to a host of different free-flying insects, where the only limitations come from the application of marker points on the wings and the magnification and speed of the cameras, which can be partially overcome by moving to different lens options.

The dragonfly (*Erythemis Simplicicollis*) was selected as the test subject for the proposed methods because it is a quad wing flier whose wings undergo considerable out of phase motion, an aerodynamically relevant characteristic (Lehmann, 2008), and also because its relatively large wings with high aspect ratios result in distinct twist and camber changes while flapping. These characteristics make it one of the most challenging insects to reconstruct digitally. It should also be noted that dragonflies are of particular interest to the authors because their extreme agility, their ability to fly with damaged wings and their ability to hover for long periods of time have lead to their emergence as a model organism for the development of micro air vehicles.

We begin the discussion of our methods with an overview of the high-speed photogrammetry system that was used to capture the dragonfly's motion in multiple 2D image planes and a conceptual look at the projection equations used to convert corresponding points in these images into a 3D coordinate space. Next, a brief explanation of how specimens were selected and prepared for filming is presented. A novel template-based hierarchical subdivision surface method for 3D wing reconstruction is then introduced. Specifically, Catmull-Clark subdivision surfaces were chosen as the cubic spline surface representation due to their ability to generate smooth surfaces from meshes of arbitrary topology. Reconstruction accuracy is then validated by projecting the reconstructed wings back into image space and comparing their outlines with expert segmentations of the wings in the original image data.

In the latter portion of the paper, the focus shifts to making consistent measurements of the time resolved wing deformations captured by the reconstruction algorithm. A least squares plane is proposed as a reference plane comparable to the rigid wing assumptions that are often introduced when quantifying wing kinematics. Metrics for wing camber and twist in the chord-wise and span-wise directions are then defined relative to the aforementioned least squares plane. An in-depth look at the time history of a wing's

deformation during a stroke is presented and detailed visualizations of wing twist and camber are shown at several instants in time. The paper concludes by proposing a novel method to incorporate wing corrugation into the reconstruction by displacement mapping morphological surface details measured from static wings onto the flapping wings.

MATERIALS AND METHODS

Object surface geometry has been defined on the macro, meso and micro structure levels based on the amount of detail present (Szirmay-Kalos and Umenhoffer, 2008). In the context of insect wing reconstruction we will use the terms macrosurface, mesosurface and microsurface to refer to the amount of detail captured by an insect wing reconstruction. The macrosurface of a reconstructed wing captures the kinematics as well as the deformations such as twist and camber undergone by the flapping wing. The mesosurface incorporates surface roughness details such as corrugation into the model. The microsurface captures tiny surface details not visible to the human eye, which we are not interested in for the purposes of this study.

This section details the first portion of the 3D wing surface reconstruction algorithm where the wing macrosurfaces are captured digitally. Dragonflies are first recorded in free-flight by a photogrammetry system. Corresponding wing points from multiple calibrated cameras are projected into world space coordinates where subdivision surface wing templates are aligned to them. The resulting reconstructed surfaces are projected back into image space and compared with expert segmentations to evaluate accuracy. The key characteristics of the system as a whole is that it requires relatively few marker points per wing while still capturing wing twist and camber. Later in the discussion section we propose a second phase of the reconstruction algorithm where mesosurface details, such as wing corrugation, will be incorporated into the model in the future.

High-Speed Photogrammetry

The photogrammetry setup used for dragonfly image collection consists of three synchronized Photron FASTCAM SA3 60K high-speed cameras with 1024×1024 pixel resolution. They were aligned orthogonal to each other on an optical table and operated at 1000 Hz with at least a 1/20000 sec. shutter speed to capture the dragonfly flight videos.

The dragonflies were illuminated by 3 halogen photo optic lamps (OSRAM, 54428). The cameras were positioned 1.5 meters away from the insects, giving a depth of field of 3-4 body lengths in all directions depending on the size of the specimen. Given that the dragonflies flap at approximately 42 Hz, this provides good temporal and spatial resolution. A comparison between the setup used for this study and those used in the most recent 3D reconstructions of insect flight is listed in Table 1.

	Insect species	Filming frequency (fps)	Wing beating frequency (Hz)	Image resolution
Walker et al. (2009b)	Locust	974	19	1024×1024
Walker et al. (2009b)	Hoverfly	4000	160	1024×512
Ristroph et al. (2009)	Fruitfly	8000	250	512×512
Fontaine et al. (2009)	Fruitfly	6000	250	512×512
Liu et al. (2008)	Dronefly	5000	164	512×320
Current study	Dragonfly	1000	42	1024×1024

Table 1. Comparison of several parameters from the current study and previous works on photogrammetry based insect flight reconstruction.

Our photogrammetry setup can be generalized to capture longer flights while still discriminating the marker points. Ignoring camera placement and lens parameters for simplicity, the cameras are limited by pixel resolution. The minimum marker point size is 1 pixel by 1 pixel. Assuming the marker points to be 500 um and the average body length of a dragonfly to be 4cm, the maximum possible field of view without moving to other camera options is 12.8 body lengths. However, the amount of wing strokes that can be captured at one time is also dependent on the flight path and speed.
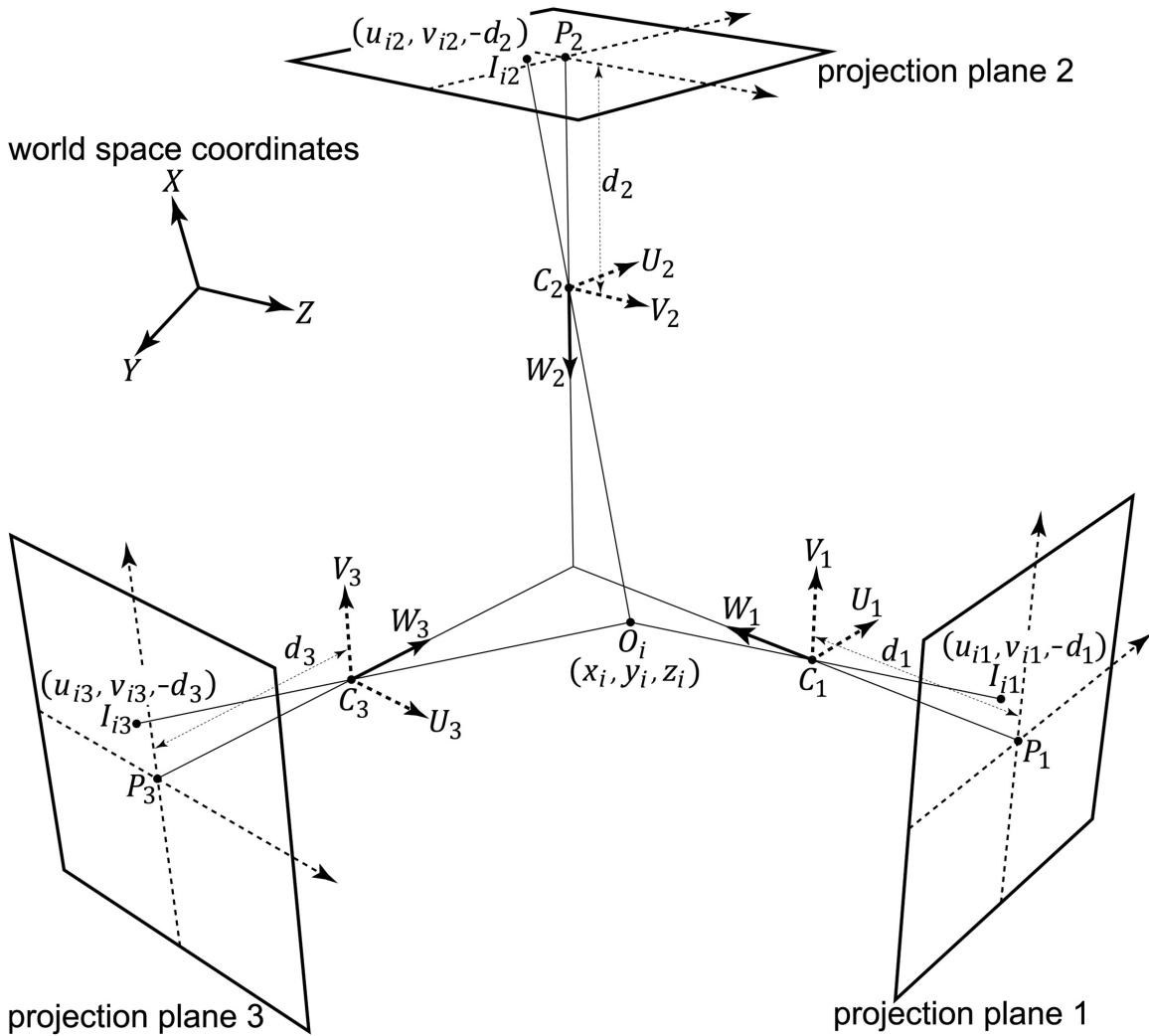
Fig. 1. Conceptual model of the photogrammetry system used to reconstruct dragonflies in free-flight.

The cameras are linked using a hardware tether and synchronized using a master-slave system with a camera response time in the nanosecond range. They are triggered by a laser controller that transmits a 5 volt TTL signal to the system, which saves a portion of data from pre- and post-trigger. The laser trigger system is a custom designed circuit that uses the open-source Arduino microcontroller platform to control all three cameras. Common laser diodes are used to provide focused beams of light to opposing light sensitive resistors. At the intersection of these two laser beams, all cameras are focused, allowing a free flying insect to trigger the cameras by interrupting both beams simultaneously. This trigger system removes nearly all human error associated with

triggering the cameras and minimizes human contact with the insects being observed. By automatically detecting when the subject is in optimum range, the current photogrammetry system is able to collect data that is consistently in focus. Useable segments of video are identified for reconstruction based on image quality and relevance of maneuver.

Fig. 1 shows a model of the perspective projections in the photogrammetric system used to estimate the 3D world coordinates of a point on a dragonfly's wing by finding its location in multiple projection planes. Generalizing the system, images are recorded with $j = 1, \ldots, n$ cameras and $i = 1, \ldots, m$ object points O_i in world coordinate space are mapped to image points I_{ij} in the corresponding projection planes. The lines connecting each object point and the corresponding image point pass through the camera's perspective center C_j.

The world coordinate system $\{X, Y, Z\}$ has its origin at an arbitrary point in space, and the image coordinate system corresponding to the $j'th$ camera $\{U_j, V_j, W_j\}$ has its origin at C_j. The coordinates of object point O_i are (x_i, y_i, z_i) in the world frame and the coordinates of the corresponding image point I_{ij} are $(u_{ij}, v_{ij}, -d_j)$ in the image frame. The world coordinates of the perspective center C_j are (x_{0j}, y_{0j}, z_{0j}). The principal axis is the line connecting the perspective center C_j and the corresponding projection plane such that it is parallel to axis W_j of the image frame, and principal point P_j is the point where it intersects the image frame. The principal distance d_j is the distance between points P_j and C_j. The image frame coordinates of the principal point are $(0, 0, -d_j)$.

In this system, the points O_i, C_j and I_{ij} are collinear for each i and j. This is the collinearity condition, which forms the basis for direct linear transform (DLT) camera calibration. Given a 3×3 rotation matrix R_j, with entries r_{j11}, r_{j12}, etc., that maps between the world space reference frame and the image space reference frame of the $j'th$ camera we can then write the collinearity equations as follows:

$$u_{ij} = \frac{-d_j(r_{j11}(x_i - x_{0j}) + r_{j12}(y_i - y_{0j}) + r_{j13}(z_i - z_{0j}))}{(r_{j31}(x_i - x_{0j}) + r_{j32}(y_i - y_{0j}) + r_{j33}(z_i - z_{0j}))} \quad (1)$$

$$v_{ij} = \frac{-d_j(r_{j21}(x_i - x_{0j}) + r_{j22}(y_i - y_{0j}) + r_{j23}(z_i - z_{0j}))}{(r_{j31}(x_i - x_{0j}) + r_{j32}(y_i - y_{0j}) + r_{j33}(z_i - z_{0j}))} \quad (2)$$

The collinearity equations allow us to determine a ray in the world coordinate system that a point must lie on given its location in the image coordinate system. When two cameras are used, the true world space location of a point can be determined by finding the intersection of the two resulting rays, however accuracy is increased if more than two cameras are used.

In order to determine several intrinsic and extrinsic parameters of each camera required by the collinearity equations (the rotation matrix R_j, the principal distance d_j and the perspective center C_j), camera calibration is performed for each camera. Camera calibration requires a set of known geometric relationships between a group of target points in the world coordinate frame. The calibration rig used for this is a 3D solid with marked points imprinted along its surface. The device was manufactured using a 3D Systems ProJet HD-3000 rapid prototyping machine, capable of printing with a resolution of 0.025 mm. The marker points on the calibration rig are manually digitized and then refined with sub pixel accuracy based on the neighboring grey values. Given at least 6 marker point correspondences, the DLT algorithm is used for calibration. Experiments showed that incorporating higher order optical and tangential distortion parameters had a negligible effect on the results, so they were removed in order to simplify the calibration process. For a more detailed explanation of the DLT method see (Abdel-Aziz and Karara, 1971).

In order to gauge calibration accuracy with respect to the world coordinate system we first reconstructed the 3D coordinates of the points on our calibration object. The discrepancy between the reconstructed 3D points and the known locations of the 3D points on the calibration object was then calculated. Our tests showed an average discrepancy of 0.1382±0.0684 mm. More information on this and other calibration accuracy metrics can be found in (Salvi et al., 2002).

3D Surface Reconstruction

This section details the steps taken to generate a 3D reconstruction of a free-flying dragonfly's body and wings based on data gathered from the aforementioned photogrammetry system. In our experience, dragonflies that are tethered to a solid object in any way do significant damage to their bodies while trying to escape. With the lack of detailed metrics to compare tethered and free-flying deformable wing kinematics, we cannot determine to what degree tethered dragonflies adequately capture true in-flight wing kinematics even if the tethered insect appears to be in a typical flight posture.

Free-flying insects present many reconstruction challenges not present when dealing with tethered insects due to the fact that the insect's translation distances and Euler angles are not held constant. Thus, camera angles and focal points in the photogrammetry system cannot be chosen based on a constant desirable position and rotation of the insect's body. Also, marker points placed on the wings and natural landmarks will not pass through approximately the same position in space at the same time during consecutive wing beats. Dealing with quad-winged insects further complicates the process due to the increased likelihood of wing overlap from one or more camera angles.

Individual dragonflies were selected for this study based on the condition of their wings, and flight experiments were started within one hour of capture. The data presented in this paper is from Eastern Pondhawk, *Erythimus Simplicicollis,* dragonflies, which were taken from a lake near the research lab during the period of August–September 2010 and 2011. The mean body mass of the specimen used to demonstrate our reconstruction was 0.265±0.0005 g, and the forewing and hindwing lengths were 35.03±0.005 mm and 33.21±0.005 mm respectively. The mid-span chord lengths for forewing and hindwing were 7.39±0.005 mm and 9.21±0.005 mm respectively.

Prior to photographing, the forewings and hindwings were each marked in a grid pattern with 15 black ink marker points of approximately 0.5 mm diameter on each forewing and 16 on each hindwing. Marker points were spaced 5.3 mm apart with a spacing accuracy of 0.6 mm in the span-wise direction and 3.6 mm apart with a spacing accuracy of 0.8 mm in the chord-wise direction. The marker points aid in reconstructing the wings in 3D because the subtle natural pattern of wing veins is indiscernible at most

time steps. The marker points were applied with a felt-tipped ink pen, adding negligible mass to the insect wings.

The initial 3D wing template models were generated with Catmull-Clark subdivision surfaces by aligning surface points corresponding to the first level of the subdivision surface hierarchy with the marker points on the wings in a top down image. The dragonfly's body was manually created with Autodesk Maya based on several still images of the dragonfly taken with calibrated cameras, and was assumed rigid due to how slowly it moves relative to the wings. Fig. 2 shows an initial configuration of a dragonfly's wings and body based on a top down view prior to takeoff.
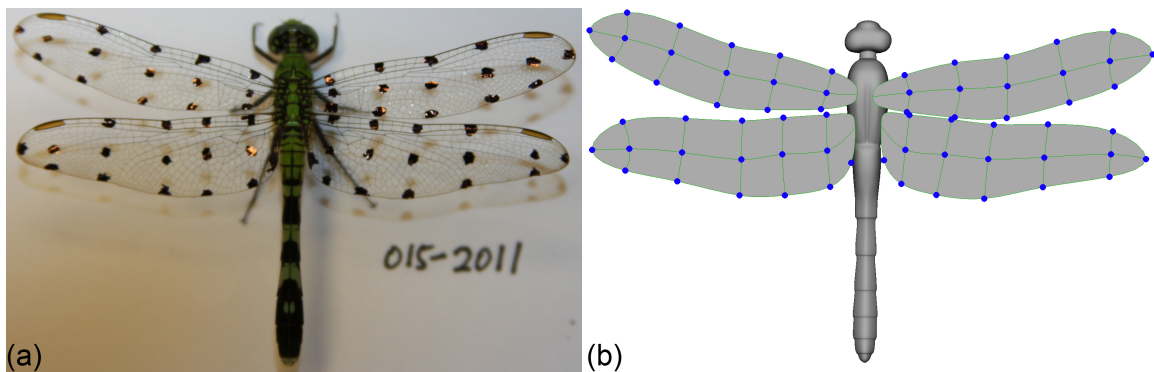

(a)　　　　　　　　　　　　　　　　　　　(b)

Fig. 2. Initial configuration of a dragonfly template mesh: (a) Top down image showing the marker points on the wings. (b) Wing and body template models with the surface points corresponding to the top level of the subdivision hierarchy marked in blue.

Cubic spline curves have already been used to reconstruct features on the surface of a deforming insect wing (Walker et al., 2009b). Our approach is an extension of this concept to the reconstruction of entire wing surfaces in order to further minimize the number of marker points required to capture both wing twist and camber. Catmull-Clark subdivision surfaces (Catmull and Clark, 1978) were chosen as the specific cubic spline surface representation due to their ability to generate smooth surfaces from meshes of arbitrary topology (Stam, 1998). Thus, the placement of marker points on an insect's wings can be based solely on best capturing the true wing deformation within the available resolution, while ignoring surface interpolation limitations.

Once the initial wing template surfaces have been created, marker points are digitized in each image recorded with the high-speed cameras at each time step. The 3D locations of each marker point that can be identified in two or more images are then determined based on the aforementioned projection equations. The vertices on the smooth wing template surfaces corresponding to the first level of the subdivision surface hierarchy are then iteratively aligned to the 3D projections of each marker point until further iterations produce no additional change in the reconstructed wing surface. Since marker points are available on both the interior of the wing and the edges, an approximation of the true 3D macrosurface shape of the wings as they bend and twist is captured with the smooth parametric surface representation. At time steps where the wings rotate such that the location of a marker points is not discernable in two or more images, 3D projections of the marker point in question were performed at adjacent time steps and B-spline interpolation was used to estimate the 3D location of the missing points at the unclear time steps. This occurred in 4.8% of marker moments.

The dragonfly's body template mesh was animated by aligning the projection of its outer border to the silhouette of the body in the images, however the body moves very slowly compared to the wings, so its reconstruction is trivial in comparison. A skilled operator working continuously can reconstruct a complete stroke for one wing in about one hour. The wing reconstruction process is somewhat labor intensive, but it is currently the only attempt at reconstructing a deformable, quad-wing insect in free-flight.

Fig. 3 shows the projection of the reconstructed wing template meshes back into image space at a point where multiple wings are undergoing a large amount of deformation. The alignment with the original data is clearly superior to methods that employ rigid wing assumptions. In total we reconstructed 5 free-flying dragonflies with this method for at least five and at most nine wing beats depending how long each dragonfly stayed in view. Analysis of kinematic variation for different flying modes within and between multiple specimens will be presented in separate papers. An animated reconstructed dragonfly can be seen in Movie 1 in the supplementary material.
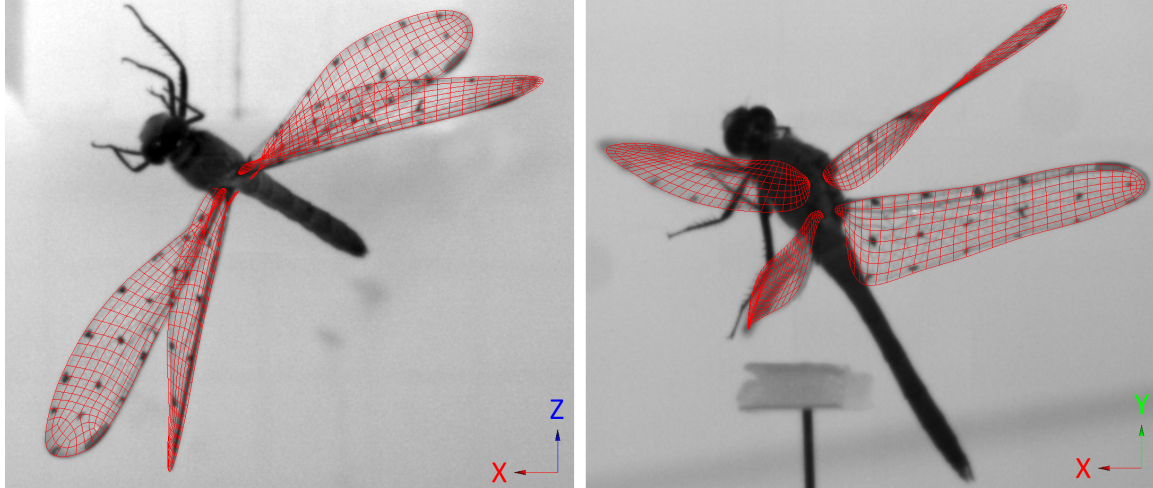
Fig. 3. Reconstructed wings projected back onto the corresponding images from the high-speed cameras at a time step where a large amount of twist and camber is present in multiple wings. The insect in this example is taking off from a pedestal, which we believe mimics a natural takeoff where the environment does not interfere with the wing kinematics more than taking off from a flat solid surface would.

Reconstruction Accuracy Evaluation

In order to gauge the accuracy of the subdivision surface interpolation when interpolating between the marker points on the wings, expert segmentations were generated by manually tracing the wings in a sampling of the original images. Also, the reconstructed wings were projected back into each image space, based on the collinearity equations. These segmentations and projections were then compared at corresponding time steps. Each pixel in the 2D projection of the reconstructed wings can then be classified as being either a true positive (T_{pos}), true negative (T_{neg}), false positive (F_{pos}) or false negative (F_{neg}) based on whether it matches the expert segmentations. The accuracy a_t at time t is defined as follows:

$$a_t = \frac{\sum T_{pos}}{\sum(T_{pos} + F_{pos} + F_{neg})} \tag{3}$$

True negative pixel classifications were ignored so as not to artificially inflate the accuracy due to the large image size. Since the expert segmentations are manually traced and not limited to interpolating between a small number of sample points, they are

14

assumed to represent the true wing borders. This accuracy metric measures how close the projected borders of the reconstructed wings match the expert segmentations, however the vertices on the interior portion of the wings were aligned to the marker points in the images in the same fashion and the same parametric surface interpolates between them, so this metric is a good indicator of the overall accuracy of the 3D reconstruction method. Fig. 4 shows an example of the pixel classifications for a set of reconstructed wings.
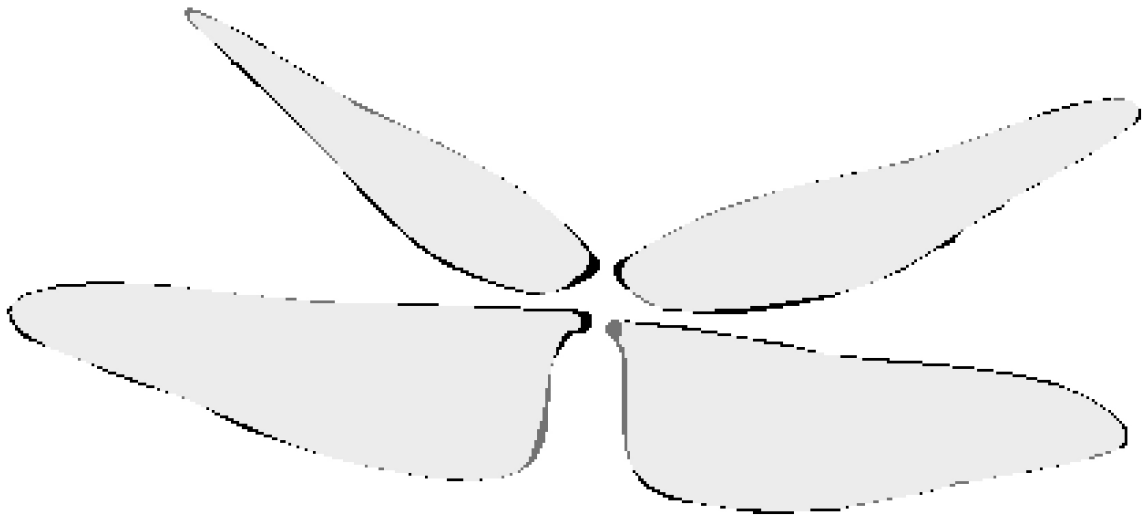
Fig. 4. Comparison between the projection of the reconstructed wings and a manually performed expert segmentation at a single time step. True positive pixels are light grey, true negatives are white, false negatives (areas found as not belonging to the wing in the 2D projection but as belonging by the human reviewer) are dark grey and false positives (areas found as belonging to the wing in the projection but not by the reviewer) are black.

Using this accuracy metric, comparisons were done between our reconstructions and rigid wing reconstructions. Rigid wing templates were aligned with the plane generated from the 3D projections of the wing root and the two marker points nearest the 75% chord on the leading edge and the 50% chord on the trailing edge. Table 2 contains average accuracy measures for each wing using each reconstruction method. Clearly the deforming wings align with the expert segmentations more consistently than the rigid wings.

	Deformable Wing Accuracy	Rigid Wing Accuracy
Right Forewing	0.9524±0.0116	0.7780±0.0869
Right Hindwing	0.9636±0.0095	0.8057±0.0375
Left Forewing	0.9399±0.0153	0.7198±0.1258
Left Hindwing	0.9549±0.0185	0.7747±0.0660

Table 2. Comparison of reconstruction accuracy a_t means and standard deviations measured from 50 consecutive time steps for each wing using both our deformable wing reconstruction method and a rigid wing reconstruction.

RESULTS

The previously discussed subdivision surface reconstruction method allows us to accurately recreate the macrosurface deformations undergone by free-flying insect wings. This section details a new approach to quantifying the deformations observed in the reconstructed wing macrosurfaces and presents an in depth analysis of a dragonfly's hindwing as an example of the methodology.

In order to accurately make repeatable measurements of the deformations, such as twist and camber, undergone by a reconstructed flapping insect wing, a universal reference plane must be established. Some works have attempted to do this by defining wing deformation with respect to a plane that is fixed to several points on the wing or with respect to the straight line between wing root and tip. However, these methods do not account for span-wise deformations and will vary based on wing size and shape. We address this by defining a least-squares plane as a universal reference plane for each wing that can aid in describing the physical position of the wing at any point in the stroke from a statistical perspective.

Wing Deformation Metrics

To study the deformation and topography of an individual wing surface Π, a least squares reference plane Ω is generated from the points on the reconstructed wing. The wing surface Π is first discretized as an element set $\{(X_l, A_l): l = 1,2, ..., m\}$, with

$X_l = (x_l, y_l, z_l)$ and A_l standing for the centroid and area of the lth element respectively. The centroid of the entire wing is defined as follows:

$$X_0 = \left(\sum_{l=1}^{m} X_l A_l\right) / \left(\sum_{l=1}^{m} A_l\right) = (x_0, y_0, z_0) \tag{4}$$

The least squares plane corresponding to the wing surface is then defined as the plane passing through centroid X_0 with unit normal vector $\boldsymbol{n}$, such that the following quantity e_0^2 is minimized:

$$e_0^2 = \sum_{l=1}^{m} |A_l^2 (X_l - X_0)\boldsymbol{n}^T|^2 = \boldsymbol{n}^T \sum_{l=1}^{m} A_l^2 (X_l - X_0)(X_l - X_0)^T \boldsymbol{n} = \boldsymbol{n}^T M \boldsymbol{n} \tag{5}$$

The symmetric matrix M in equation 5 is the central moments tensor. The components of normal vector $\boldsymbol{n}$ can be found as the principal axes of inertia of M after singular value decomposition is applied. More details on this least squares plane-fitting method can be found in (Ahn, 2004).

The obtained least squares plane Ω and reconstructed wing surface Π, shown in Fig. 5, are used together to define several wing deformation metrics such as the local angle of twist, the span-wise camber and the chord-wise camber. Points A and B on Ω denote the projections of the user selected wing root and tip onto Ω. The cross-section plane χ_k can then be defined normal to line segment AB, where the subscript k denotes the percentage of the distance between points A and B. Lower values of k indicate cuts taken close to the root of the wing, and higher values indicate cuts taken near the wing tip.

The camber line S_k is defined as the intersection of the plane χ_k and the wing surface Π. The chord C_k is then the line segment connecting the trailing and leading points of S_k. The line l_k is then defined as the intersection of Ω and χ_k. The local angle of chord-wise twist α_k^c at the cross-section plane χ_k can then be defined as the angle between the chord C_k and line l_k. These definitions are explained visually in Fig. 5.

A similar process is used to define deformation metrics in the span-wise direction. The superscript c denotes a cross-sectional cut in the chord-wise direction and the superscript s denotes one in the span-wise direction. Instead of using points A and B to define a line along which cross section planes are placed, the projection of the endpoints of C_{50} onto Ω is used. Thus, the span P_k and local angle of span-wise twist α_k^s can be measured relative to Ω in cuts approximately parallel to the leading edge of the wing.

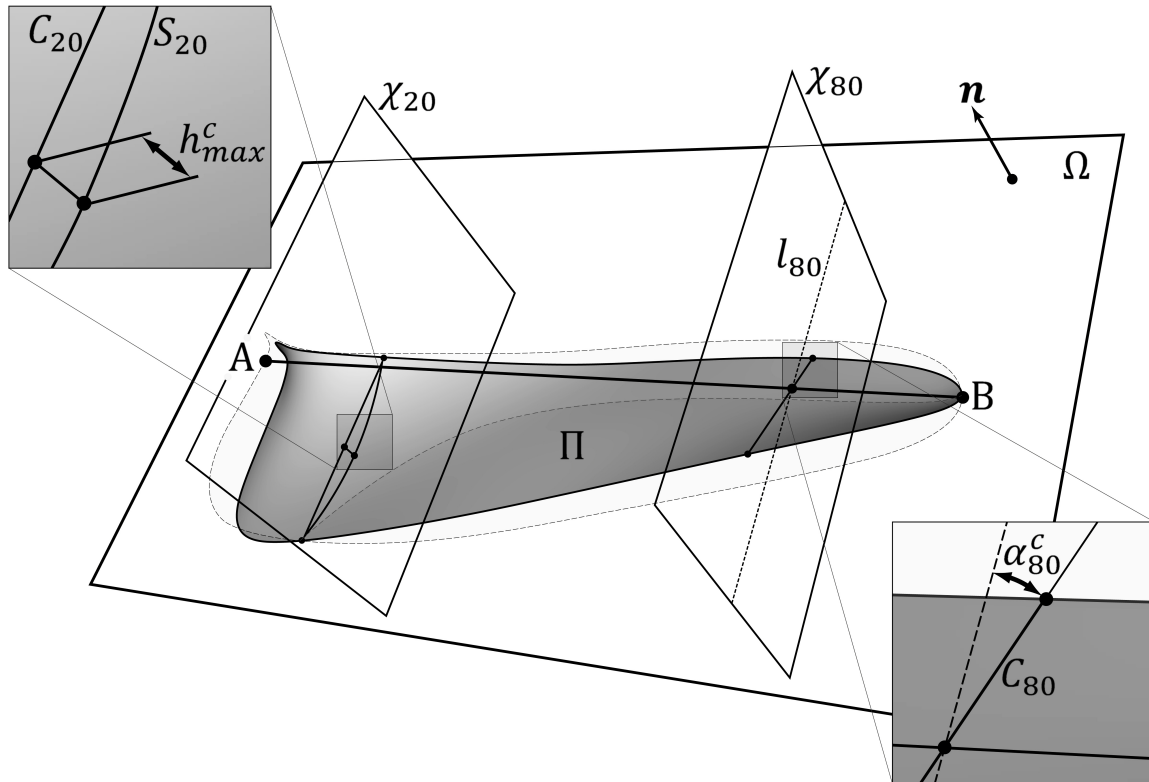Fig. 5. Conceptual illustration of wing deformation measurements taken in the chord-wise direction with respect to the least squares plane Ω. The local angle of chord-wise twist α_k^c is illustrated at the cross-section plane 80% from the wing root and the camber-to-chord ratio parameters are illustrated in the cross-section 20% from the root. The grey dotted silhouette of the wing is the projection of the entire deformed wing onto the least squares plane.

Wing Deformation Analysis

To illustrate the subtle variations in instantaneous wing deformation captured by our reconstruction method, we have used the aforementioned metrics to perform a detailed

analysis of the right hindwing of a dragonfly. In the future we plan to combine these measurements with CFD results to further explain their causes. The camber lines S_k, cut in chord-wise and span-wise directions, were sampled at 10% increments.
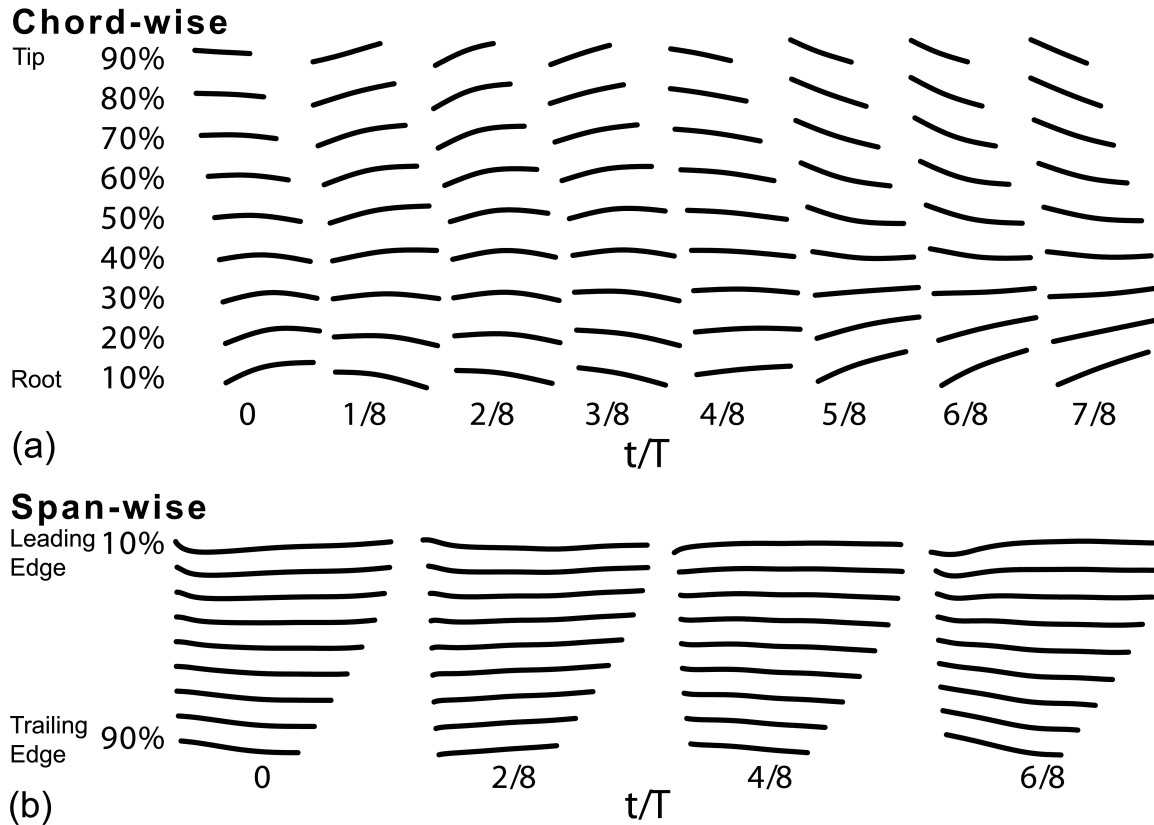

(a)

(b)

Fig. 6: Visualization of sectioned cuts of the camber lines along the right hindwing for one full stroke starting with the downstroke. The viewing angle for each cut is held perpendicular to the corresponding cross-section plane χ_k and the camera's up vector is normal to the least squares plane Ω. (a) Chord-wise cuts. (b) Span-wise cuts.

At the start of the downstroke, there is a larger amount of camber present near the wing root (Fig. 6a, t/T=0-2/8). However, the wing becomes increasingly flat as the measurements progress along the wingspan approaching to the wing tip. As the stroke progresses, the wing shows only small amounts of camber change near the tip (Fig. 6a, t/T=3/8). As the wing reaches stroke reversal, it is at the most flattened state (Fig. 6a, t/T=4/8). Following reversal, the wing shows considerable twisting motion during the upstroke with little camber produced (Fig. 6a, t/T=5/8-7/8).

In Fig. 6b, span-wise cuts of the right hindwing are shown as a function of chord-wise distance at different time instants during one wing beat. The 10% cuts occur nearest the leading edge and 90% nearest the trailing edge of the wing. The maximum span-wise camber occurs near the leading edge during downstroke, due to flexing against the airflow and the wakes formed in the upstroke.

Fig. 7 reveals a more quantitative look at wing camber with the camber-to-chord ratios (Fig. 7a) and camber-to-span ratios (Fig. 7b). The maximum camber height at a cross section of a wing is denoted by h_{max}^c in the chord-wise direction and h_{max}^s in the span-wise direction. Thus, the camber-to-chord ratio is defined as h_{max}^c/C_k or h_{max}^s/P_k in the span-wise case. This measurement reveals the relative camber throughout the wing as a function of time during the wing beat.

The stroke is divided into downstroke and upstroke with the stroke reversal marked by the dashed-line. Note that stroke reversal does not occur at the half-way point of the cycle, with the downstroke being slightly faster than the upstroke. Fig. 7a shows that chord-wise camber is most prominent near the wing root at the beginning of the downstroke. Combined with the negative span-wise camber shown in Fig. 7b, it suggests a cup-like wing deformation, which is expected as the wing flexes against the airflow.

One particularly interesting feature of the data in Fig. 7a is the two peaks in camber-to-chord ratio on the root half of the wing (10%, 30% and 50% cuts) during the downstroke. The first peak is at the very beginning of the downstroke. As the downstroke progresses, the wing begins to flatten, and then the camber reforms.

It is widely accepted that flapping insect wings are primarily passive structures. Combes and Daniel noted that insect flight muscles are restricted to the wing base, so free-flying insects have less active control over the deformation undergone by their wings than do other flapping fliers such as birds or bats (Combes and Daniel, 2003a). However, Simmons noted that the base of a dragonfly's wing has the musculature and neural control to actively flex and distort itself nearest the root (Simmons, 1977). The presence of multiple local maxima during the downstroke in Fig. 7a could be a result of active camber control near the wing root or the inertial effect due to the wing deceleration or

both. Further study involving CFD results will be needed to investigate this phenomena that was identified with the more detailed wing reconstructions and measurements.
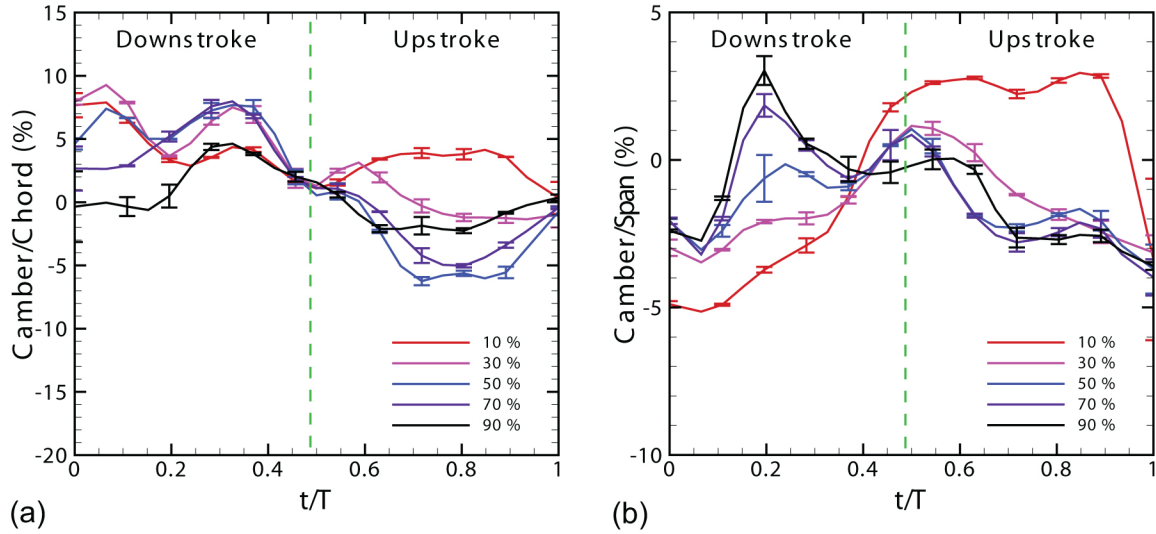

(a)

(b)

Fig. 7: Camber ratios of the right hindwing plotted over time for one stroke. Stroke reversal is marked by the vertical dotted line. (a) Camber in the chord-wise direction. (b) Camber in the span-wise direction.

Fig. 7a also shows that as the downstroke completes, the chord-wise camber is near zero, indicating that the wing is almost completely flat in the chord-wise direction. This is not true in the span-wise direction. At stroke reversal, the span-wise camber closest to the leading edge is near its peak. This can be explained by the inertial loading at stroke reversal, where the leading edge, which is the most dense and rigid portion of the wing, decelerates abruptly. Changing directions of wing stroke causes the positive camber. This trend is present in span-wise camber throughout the entire cycle, where the camber nearest the leading edge is caused predominantly by inertial loading in tandem with abrupt accelerations and decelerations at stroke reversal.

Our reconstruction method also captures how insect wings twist while flapping. Fig. 8 shows the local twist angle α_k in both the chord-wise and span-wise directions. It is clear that chord-wise twisting is relatively constant in the upstroke of the right hindwing. On the other hand twist varies near both the wing root and the wing tip during the downstroke. This is most likely due to the faster speed of the downstroke and the

incidence of the wing with the wake formed in the previous stroke. To provide more clues as to why the downstroke sees changes in both camber and twist, more wing beat cycles will be analyzed in the future along with force histories of the wing beats.

It can also be noted from Fig. 8b that the twisting axis occurs at roughly 30% of the distance between the leading and trailing edge. At this distance, the twist angle along the span is closest to zero, making it the logical axis about which the wing would twist as a whole. In order to quantify the impact that slight differences in marker point identification in the reconstruction process have on the camber and twist measurements, eight different human operators performed reconstructions of the wing measured in Figs 7 and 8. The differences in the resulting reconstructions were used to generate the error bars in these figures, however the overall trends were unchanged.
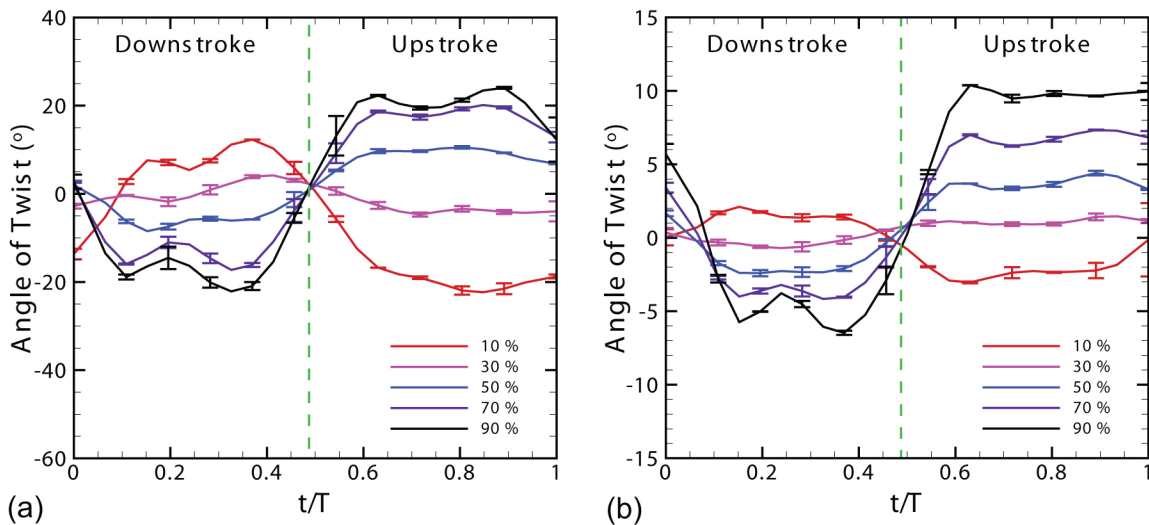

Fig. 8: Local angle of twist of the right hindwing plotted over time for one stroke. Stroke reversal is marked by the vertical dotted line. (a) Twist in the chord-wise direction. (b) Twist in the span-wise direction.

To further elucidate the deformation of the wing, visualizations of the right hindwing were created by mapping the distance from the least squares reference plane Ω to the color of the wing surface (Fig. 9). When using this method to visualize wing twist, the viewing direction is chosen perpendicular to the least squares plane with the focal point on the wing centroid X_0 in order to facilitate side-by-side comparisons at different

portions of the stroke. At the minimum twisted wing shows mainly concavity, whereas the maximum twisted wing shows a more modal display of distance from the plane.
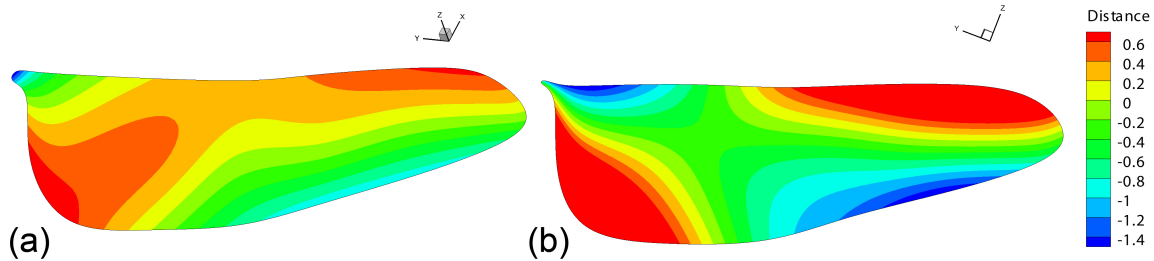

Fig. 9: Color mapping used to visualize instantaneous wing deformation in the right hindwing. The distance between the wing and the least squares plane Ω is measured in mm. (a) Minimum twist occurring at a downstroke to upstroke reversal. (b) Maximum twist occurring at the end of an upstroke.

In the case of the right hindwing (Figs 8, 9), the twisting helps to form and hold the camber of the wing before stroke reversal. At the instant of reversal, the twisting and camber diminish, resulting in the least deformed wing surface. As the following upstroke progresses, the local angle of twist changes suddenly (Fig. 8), which induces camber once again. This pattern repeats itself, helping to explain the relationship between twist and camber. It is also worth mentioning that the quantified twist angle and its variation along the span-wise direction can be an indication of passive (Ennos 1988, Bergou et al. 2007) or active (Weis-Fogh 1973) wing pitch, once combined with the information of the aerodynamic and inertial forces/torques and associated power (Bergou et al. 2007). Detailed study on the passive or active wing pitch will be left to future work, which in turn can shed a light on the causes of wing deformation.

DISCUSSION

Thus far we have demonstrated a reconstruction method capable of capturing the detailed deformations undergone by free-flying insect wings and several metrics for consistently analyzing the resulting wing surfaces. A photogrammetry system consisting of three high-speed calibrated cameras is used to capture free-flying insects, whose wings have been marked in a grid pattern. The marker points are digitized and projected into a

world coordinate system at each recorded time step, where a Catmull-Clark subdivision surface is aligned to them. A least squares plane is then generated for each reconstructed wing surface at each time step. Chord-wise and span-wise camber and wing twist are then consistently measured relative to this plane at different slices through the wing.

The main strength of the presented methodology is that no rigid wing assumptions are made in either the reconstruction or the deformation analysis. The subdivision surface parameterization was demonstrated to effectively capture wing deformation between marker points, thus requiring fewer overall marker points, which is very desirable when trying to digitize multiple points on overlapping wings. At the same time it is general enough to allow for arbitrarily placed marker points on wings with varying aspect ratios and natural markings. Similarly, using the least squares plane to define wing twist and camber adds generality to the methodology so that it can be used effectively regardless of the amount of deformation undergone by the insect's wings.

We zeroed in on a single flap of a single wing in order to identify the subtle deformations occurring at different parts of the wing at different times in the stroke. Multiple visualization methods were demonstrated to identify wing deformations. Images of curves resulting from the chords and spans being projected onto cross sectional planes convey detailed deformations at single instants in time (Fig. 6). Similarly, mapping wing twist to surface color shows a complete picture of how a wing is twisting at a single time step (Fig. 9). Time histories of chamber to chord ratio and local angle of twist in the span-wise and chord-wise directions were used to track deformation changes at different points in the wing stroke. This allowed us to identify a particularly interesting double peak in the chord-wise camber near the wing root, which suggests that the dragonfly could actively be flexing the muscles at the hindwing root to induce camber. Another possible cause is the inertial effect due to the wing deceleration. This phenomenon will require further validation between many specimens.

Digital reconstruction of free-flying insect wings still has many potential options for improvement. We close our discussion with the proposal of a method to model corrugation in free-flying insect wings, which we plan to explore in more detail in the future.

Mesosurface Reconstruction

The 3D wing reconstruction algorithm and deformation metrics discussed thus far have all focused on the macrostructure of the wings. Capturing the information necessary to reconstruct mesosurface details like wing corrugation directly from the output of a high-speed camera system is extremely challenging. Either individual wing veins must be tracked at each time step or a very large number of marker points must be employed. For instance, (Walker et al., 2009b) used approximately 100 marker points per tethered locust hindwing in order to capture the most distinct wing veins. We believe it is not feasible or desirable to track the very high amount of marker points needed to reconstruct the mesosurface details of free flying insect wings, especially if one is interested in quad wing insects.

It is considerably more practical to measure the mesosurface of a static insect wing (Jongerius and Lentink, 2010;Tsuyuki et al., 2006). Thus, our approach is to build on this work in order to model the surface corrugation of reconstructed free-flying insect wings. Instead of tracking the wing corrugation details at each time step of the high-speed camera output, it is captured once from a static wing and then mapped to the reconstructed wings by means of a displacement map.

Displacement mapping is a technique commonly used in computer graphics, which uses a height map to displace the actual geometry of a surface in the direction locally normal to that surface (Fig. 10a,b). In the case of our dragonfly wings, the displacement map (Fig. 10c) used to demonstrate the technique was generated by scaling the geometric profiles described by (Kesel, 2000) to align with our specimen's wing chord.

Insect wing venation patterns can also be modeled in the final reconstruction in a similar fashion by using texture maps based on the original wing coloration. Dark colored wing veins can be automatically identified as minimum intensity ridgelines, which are extracted from a top down image of the wings taken before the marker points have been applied. A stylized version of the true wing venation pattern can then be generated based on these ridgelines (Fig. 10d). The texture and displacement are then UV mapped to the wings in their initial static configuration (Figs 2a, 10). Due to the fact that the wing geometry is being displaced normal to the initial reconstructed macrosurface, the

displacement maps can then be used to project the corrugation and surface roughness onto the already deformed wings at any time step (Fig. 10b,f,g). An ambient occlusion rendering pass was used to further visually emphasize the subtle corrugation pattern on the wings (Fig. 10e).
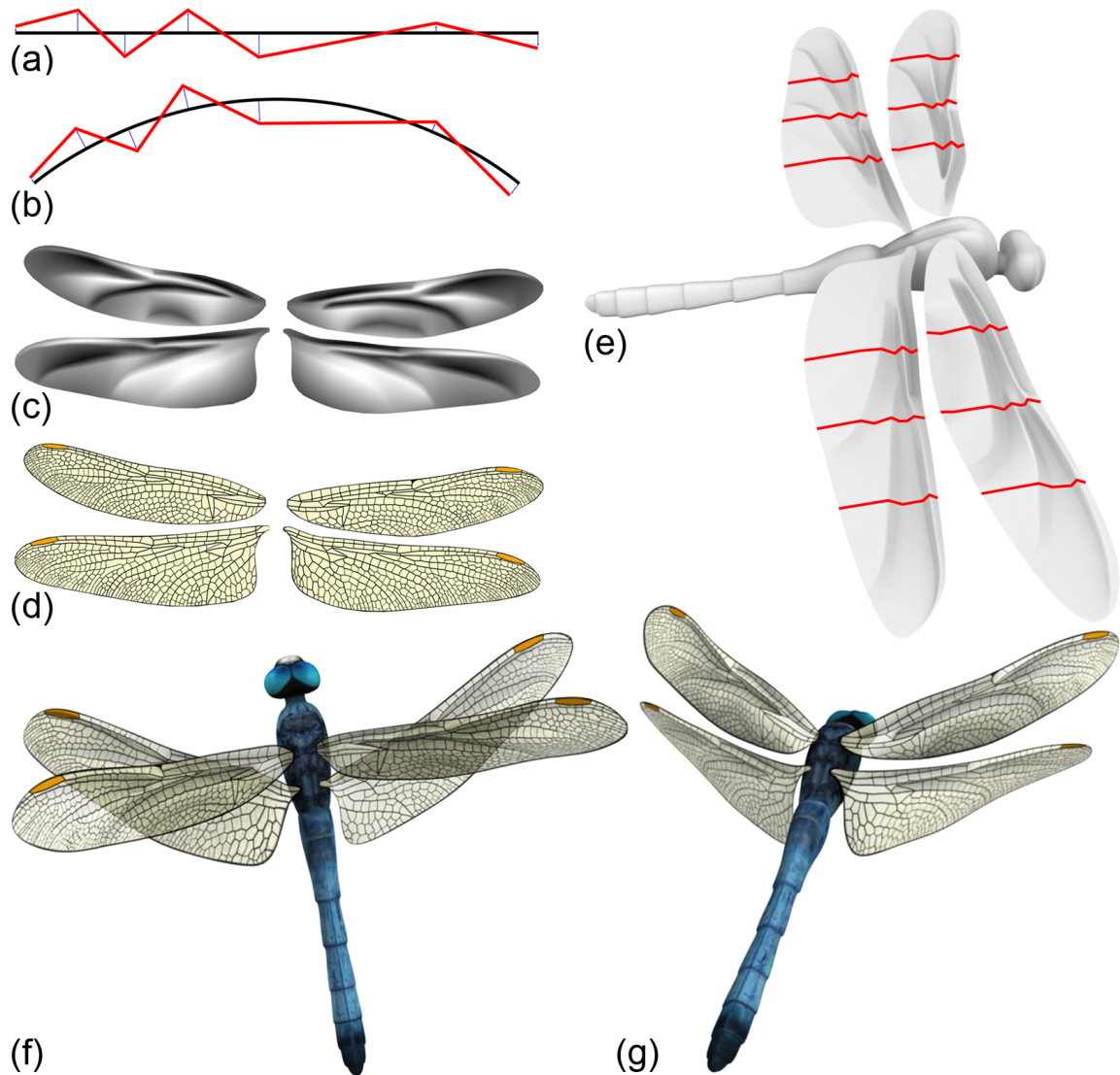
Fig. 10: Illustration of the displacement mapping method for modeling insect wing corrugation and venation. (a,b) Conceptual illustration of a 2D wing (black), displaced in its normal direction (red) in order to approximate corrugation in the initial and deformed states. (c) Displacement map approximating the wing surface corrugation measured from static dragonfly wings. (d) Stylized texture map of the wing venation pattern that was applied to the reconstructed wings as a texture and transparency map. (e) Initial configuration of the wing templates with a displacement map applied to model wing

corrugation. The corrugation at 30%, 50% and 70% cuts in the chord-wise direction is marked on each wing. (f,g) High quality perspective renderings of a reconstructed dragonfly with texture, transparency and displacement maps to facilitate improved visual perception of the twist, camber and corrugation captured by our reconstruction methods.

In the future we plan to further validate this method, however the fact that insect wings are largely passive structures suggests that displacement in the direction normal to the reconstructed macrosurface is a reasonable assumption to make when modeling wing corrugation. When compared to the aforementioned challenges with accurately reconstructing wing corrugation for free-flying insects directly from the high speed camera output or the alternative of ignoring it entirely, we believe this is the best approach to take when reconstructing free-flying insect wings. The main benefit of this approach that sets it apart from other methods is that it does not require any additional information beyond the initial marker points to be tracked in the high speed camera data in order to model wing venation and corrugation. This is an extremely important characteristic as we work towards fully automated reconstruction of the deformation and surface corrugation of free-flying insect wings.

ACKNOWLEDGEMENT

FUNDING

LIST OF SYMBOLS

j	Camera index
i	Object point index
t	Time step
O_i	Object point

I_{ij}	Image point
C_j	Perspective center
X, Y, Z	World coordinate system
U_j, V_j, W_j	Image coordinate system
P_j	Principal point
d_j	Principal distance
R_j	Rotation matrix mapping between world and image space
a_t	Reconstruction accuracy at time t
l	Reconstructed wing element index
Π	Reconstructed wing surface
Ω	Least squares reference plane for a wing
X_l	Centroid of a wing surface element
A_l	Area of a wing surface element
X_0	Centroid of an entire wing
M	Central moments tensor
$\boldsymbol{n}$	Unit vector normal to Ω
e_0^2	Minimized least squares distance
A	Wing root projected onto Ω
B	Wing tip projected onto Ω
k	Subscript denoting percentage distance between projected root and tip
χ_k	Cross section plane
S_k	Camber line
C_k	Chord line
P_k	Span line
l_k	Intersection of the cross section and least squares planes
α_k	Local angle of twist
h_{max}	Maximum camber height
c	Superscript denoting a chord-wise measurement
s	Superscript denoting a span-wise measurement

REFERENCES

Abdel-Aziz, Y. I. and Karara, H. M. (1971). Direct Linear Transformation from Comparator Coordinates into Object Space Coordinates in Close-Range Photogrammetry. **1,** 1-18.

Ahn, S. J. (2004). *Least Squares Orthogonal Distance Fitting of Curves and Surfaces in Space*, pp. 125: Springer.

Bergou, A. J., Xu, S. and Wang, Z. J. (2007). Passive Wing Pitch Reversal in Insect Flight. *Journal of Fluid Mechanics* **591,** 321-337.

Bergou, A. J., Ristroph, L., Guckenheimer, J., Cohen, I. and Wang, Z. J. (2010). Fruit Flies Modulate Passive Wing Pitching to Generate in-Flight Turns. *Physical Review Letters* **104,** 148101-1-148101-4.

Catmull, E. and Clark, J. (1978). Recursively Generated B-Spline Surfaces on Arbitrary Topological Meshes. *Computer-Aided Design* **10,** 350-355.

Combes, S. A. and Daniel, T. L. (2001). Shape, Flapping and Flexion: Wing and Fin Design for Forward Flight. *Journal of Experimental Biology* **204,** 2073-2085.

Combes, S. A. and Daniel, T. L. (2003a). Flexural Stiffness in Insect Wings I. Scaling and the Influence of Wing Venation. *Journal of Experimental Biology* **206,** 2979-2987.

Combes, S. A. and Daniel, T. L. (2003b). Flexural Stiffness in Insect Wings II. Spatial Distribution and Dynamic Wing Bending. *Journal of Experimental Biology* **206,** 2989-2997.

Dickinson, M. H., Lehmann, F. and Sane, S. P. (1999). Wing Rotation and the Aerodynamic Basis of Insect Flight. *Science* **284,** 1954-1960.

Du, G. and Sun, M. (2008). Effects of Unsteady Deformation of Flapping Wing on its Aerodynamic Forces. *Applied Mathematics and Mechanics* **29,** 731-743.

Du, G. and Sun, M. (2010). Effects of Wing Deformation on Aerodynamic Forces in Hovering Hoverflies. *Journal of Experimental Biology* **213,** 2273-2283.

Ennos, A. R. (1988). The Inertial Cause of Wing Rotation in Diptera. *Journal of Experimental Biology* **140,** 161-169.

Fontaine, E. I., Zabala, F., Dickinson, M. H. and Burdick, J. W. (2009). Wing and Body Motion during Flight Initiation in Drosophila Revealed by Automated Visual Tracking. *Journal of Experimental Biology* **212,** 1307-1323.

Hedrick, T. L. and Biewener, A. A. (2007). Low Speed Maneuvering Flight of the Rose-Breasted Cockatoo (Eolophus Roseicapillus). I. Kinematic and Neuromuscular Control of Turning. *Journal of Experimental Biology* **210,** 1897-1911.

Iriarte-Díaz, J., Riskin, D. K., Willis, D. J., Breuer, K. S. and Swartz, S. M. (2011). Whole-Body Kinematics of a Fruit Bat Reveal the Influence of Wing Inertia on Body Accelerations. *The Journal of Experimental Biology* **214,** 1546-1553.

Jongerius, S. R. and Lentink, D. (2010). Structural Analysis of a Dragonfly Wing. *Experimental Mechanics* **50,** 1323-1334.

Kesel, A. (2000). Aerodynamic Characteristics of Dragonfly Wing Sections Compared with Technical Aerofoils. *Journal of Experimental Biology* **203,** 3125-3135.

Koehler, C., Wischgoll, T., Dong, H. and Gaston, Z. (2011). Vortex Visualization in Ultra Low Reynolds Number Insect Flight. *IEEE Transactions on Visualization and Computer Graphics* **17,** 2071-2079.

Lauder, G. V., Madden, P. G. A., Mittal, R., Dong, H. and Bozkurttas, M. (2006). Locomotion with Flexible Propulsors: I. Experimental Analysis of Pectoral Fin Swimming in Sunfish. *Bioinspiration & Biomimetics* **1,** 25-34.

Lehmann, F. (2008). When Wings Touch Wakes: Understanding Locomotor Force Control by wake–wing Interference in Insect Wings. *Journal of Experimental Biology* **211,** 224-233.

Liu, Y. and Sun, M. (2008). Wing Kinematics Measurement and Aerodynamics of Hovering Droneflies. *Journal of Experimental Biology* **211,** 2014-2025.

Norberg, U. M. L. and Winter, Y. (2006). Wing Beat Kinematics of a Nectar-Feeding Bat, Glossophaga Soricina, Flying at Different Flight Speeds and Strouhal Numbers. *Journal of Experimental Biology* **209,** 3887-3897.

Ristroph, L., Berman, G. J., Bergou, A. J., Wang, Z. J. and Cohen, I. (2009). Automated Hull Reconstruction Motion Tracking (HRMT) Applied to Sideways Maneuvers of Free-Flying Insects. *Journal of Experimental Biology* **212,** 1324-1335.

Salvi, J., Armangué, X. and Batlle, J. (2002). A Comparative Review of Camera Calibrating Methods with Accuracy Evaluation. *Pattern Recognition* **35,** 1617-1635.

Sane, S. P. (2003). The Aerodynamics of Insect Flight. *Journal of Experimental Biology* **206,** 4191-4208.

Simmons, P. (1977). The Neuronal Control of Dragonfly Flight I. Anatomy. *Journal of Experimental Biology* **71,** 123-140.

Song, D., Wang, H., Zeng, L. and Yin, C. (2001). Measuring the Camber Deformation of a Dragonfly Wing using Projected Comb Fringe. *Review of Scientific Instruments* **72,** 2450-2454.

Stam, J. (1998). Exact Evaluation of Catmull-Clark Subdivision Surfaces at Arbitrary Parameter Values. *SIGGRAPH '98: Proceedings of the 25th annual conference on Computer graphics and interactive techniques* 395-404.

Stanford, B., Kurdi, M., Beran, P. and McClung, A. (2010). Shape, Structure, and Kinematic Parameterization of a Power-Optimal Hovering Wing. *51st AIAA/ASME/ASCE/AHS/ASC Structures, Structural Dynamics, and Materials Conference*.

Sunada, S., Song, D., Meng, X., Wang, H., Zeng, L. and Kawachi, K. (2002). Optical Measurement of the Deformation, Motion, and Generated Force of the Wings of a Moth, Mythimna Separata (Walker). *JSME International Journal Series B Fluids and Thermal Engineering* **45,** 836-842.

Szirmay-Kalos, L. and Umenhoffer, T. (2008). Displacement Mapping on the GPU — State of the Art. *Computer Graphics Forum* **27,** 1567-1592.

Tobalske, B. W., Warrick, D. R., Clark, C. J., Powers, D. R., Hedrick, T. L., Hyder, G. A. and Biewener, A. A. (2007). Three-Dimensional Kinematics of Hummingbird Flight. *Journal of Experimental Biology* **210,** 2368-2382.

Tsuyuki, K., Sudo, S. and Tani, J. (2006). Morphology of Insect Wings and Airflow Produced by Flapping Insects. *Journal of Intelligent Material Systems and Structures* **17,** 743-751.

Vanella, M., Fitzgerald, T., Preidikman, S., Balaras, E. and Balachandran, B. (2009). Influence of Flexibility on the Aerodynamic Performance of a Hovering Wing. *Journal of Experimental Biology* **212,** 95-105.

Walker, S. M., Thomas, A. L. R. and Taylor, G. K. (2009a). Deformable Wing Kinematics in the Desert Locust: How and Why do Camber, Twist and Topography Vary through the Stroke? *Journal of The Royal Society Interface* **6,** 735-747.

Walker, S. M., Thomas, A. L. R. and Taylor, G. K. (2009b). Photogrammetric Reconstruction of High-Resolution Surface Topographies and Deformable Wing

Kinematics of Tethered Locusts and Free-Flying Hoverflies. *Journal of The Royal Society Interface* **6,** 351-366.

Walker, S. M., Thomas, A. L. R. and Taylor, G. K. (2010). Deformable Wing Kinematics in Free-Flying Hoverflies. *Journal of The Royal Society Interface* **7,** 131-142.

Wang, H., Zeng, L., Liu, H. and Yin, C. (2003). Measuring Wing Kinematics, Flight Trajectory and Body Attitude during Forward Flight and Turning Maneuvers in Dragonflies. *Journal of Experimental Biology* **206,** 745-757.

Weis-Fogh, T. (1973). Quick Estimates of Flight Fitness in Hovering Animals, Including Novel Mechanisms for Lift Production. *Journal of Experimental Biology* **59,** 169-230.

Willmott, A. and Ellington, C. (1997). Measuring the Angle of Attack of Beating Insect Wings: Robust Three-Dimensional Reconstruction from Two-Dimensional Images. *Journal of Experimental Biology* **200,** 2693-2704.

Wootton, R. J. (1993). Leading Edge Section and Asymmetric Twisting in the Wings of Flying Butterflies. *Journal of Experimental Biology* **180,** 105-117.

Zeng, L., Hao, Q. and Kawachi, K. (2000). A Scanning Projected Line Method for Measuring a Beating Bumblebee Wing. *Optics Communications* **183,** 37-43.

Zeng, L., Matsumoto, H. and Kawachi, K. (1996). A Fringe Shadow Method for Measuring Flapping Angle and Torsional Angle of a Dragonfly Wing. *Measurement Science and Technology* **7,** 776-781.

Zhao, L., Deng, X. and Sane, S. P. (2011). Modulation of Leading Edge Vorticity and Aerodynamic Forces in Flexible Flapping Wings. *Bioinspiration & Biomimetics* **6,** 036007.

Zhao, L., Huang, Q., Deng, X. and Sane, S. P. (2009). Aerodynamic Effects of Flexibility in Flapping Wings. *Journal of The Royal Society Interface* **7,** 485-497.